



# Liberating photocarriers in mesoporous single-crystalline SrTaO<sub>2</sub>N for efficient solar water splitting

Lin Yang<sup>a,b,1</sup>, Qingyang Fu<sup>a,b,1</sup>, Lina Wang<sup>a,b</sup>, Jinxing Yu<sup>a,b</sup>, Xiaoxiang Xu<sup>a,b,\*</sup>

<sup>a</sup> Clinical and Central Lab, Putuo People's Hospital, Tongji University, Shanghai 200060, China

<sup>b</sup> Shanghai Key Lab of Chemical Assessment and Sustainability, School of Chemical Science and Engineering, Tongji University, Shanghai 200092, China

## ARTICLE INFO

### Keywords:

Topotactic conversion  
Porous single crystal  
SrTaO<sub>2</sub>N  
Photocatalyst  
Solar water splitting

## ABSTRACT

Porous single-crystalline SrTaO<sub>2</sub>N, combining structural homogeneity and high porosity, afford a great promise as an active photocatalyst. The lack of grain boundaries in SrTaO<sub>2</sub>N porous single crystals (PSCs) enables fast photocarrier migration from bulk to the surface whilst the high porosity offers adequate accessible surface to perform photocatalytic reactions. In this work, we demonstrate a facile synthesis of SrTaO<sub>2</sub>N PSCs via a topotactic conversion route. These SrTaO<sub>2</sub>N PSCs deliver exceptional activity and stability for photocatalytic O<sub>2</sub> production from water with a record-breaking apparent quantum efficiency as high as 17.9% at 420 ± 20 nm. Overall water splitting with H<sub>2</sub>/O<sub>2</sub> equals 2 has also been attained in a Z-scheme system employing SrTaO<sub>2</sub>N PSCs as the O<sub>2</sub>-evolution moiety. These results signify a paradigm to improve photocatalytic performance based on PSCs, which extends the toolbox to achieve efficient solar water splitting over conventional photocatalysts.

## 1. Introduction

H<sub>2</sub> liberation from water driven by light-illuminated photocatalysts represents a simple and sustainable means to convert solar energy into useful chemicals [1–9]. This promising technique opens up possibilities to build a clean energy infrastructure upon which we can fully decarbonize our fossil-fuel-based energy economics [10–17]. In spite of such an appealing scenario, efficient water cleavage has only been realized in some UV-illuminated wide-bandgap semiconductors [18,19], resulting in poor utilization of solar photons that dominate in the visible-light region. Developing stable narrow-bandgap semiconductors capable of water redox reactions remains a prerequisite for efficient solar water splitting. Nevertheless, water splitting over narrow bandgap semiconductors is very challenging [20]. There are competitive tensions, e.g. bandgap is narrowed at the expense of photocarrier energetics [21]. It becomes critical to maximize photocarrier transportation/transfer so as to offset the reduced energetics of photocarriers in narrow bandgap semiconductors [22].

As a typical narrow-bandgap semiconductor, SrTaO<sub>2</sub>N is a promising candidate for solar water splitting due to appropriate band edge alignments [23–25]. With an absorption edge approaching 600 nm, SrTaO<sub>2</sub>N warrants a theoretical solar-to-hydrogen conversion efficiency as high as

15% [26,27]. However, SrTaO<sub>2</sub>N normally bears a poor photocatalytic performance and is susceptible to photocatalytic self-decomposition [28–30]. This has been ascribed to the harsh synthetic environment (e.g. high-temperature ammonolysis) that produces a high concentration of defects in SrTaO<sub>2</sub>N, particularly at the interfaces like grain boundaries [24,31–37]. These interfaces are full of nonstoichiometric and/or dangling bonds which are electronically active to trap photocarriers and to promote their recombination or side reactions [31,38]. Moreover, grain boundaries are inaccessible to photochemical reactions, let alone they also break band edge continuity due to an abrupt change of crystal structure [39]. Disruption of band edge continuity creates undesired energy barriers that hinder photocarrier migration and shorten their diffusion length [40]. Thereby, how to eliminate grain boundaries is key to improve the photocatalytic performance of SrTaO<sub>2</sub>N [41].

SrTaO<sub>2</sub>N porous single crystals (PSCs), combining structural homogeneity and high porosity, afford a promising photocatalytic performance. The absence of grain boundaries in SrTaO<sub>2</sub>N PSCs enables rapid photocarrier transportation due to the removal of undesired energy barriers. The high porosity, on the other hand, provides ample reachable surface to host photocatalytic reactions [42]. Nonetheless, SrTaO<sub>2</sub>N PSCs are difficult to synthesize from conventional precursors. This is

\* Corresponding author at: Clinical and Central Lab, Putuo People's Hospital, Tongji University, Shanghai 200060, China.

E-mail address: [xxxu@tongji.edu.cn](mailto:xxxu@tongji.edu.cn) (X. Xu).

<sup>1</sup> These authors contribute equally to this work.

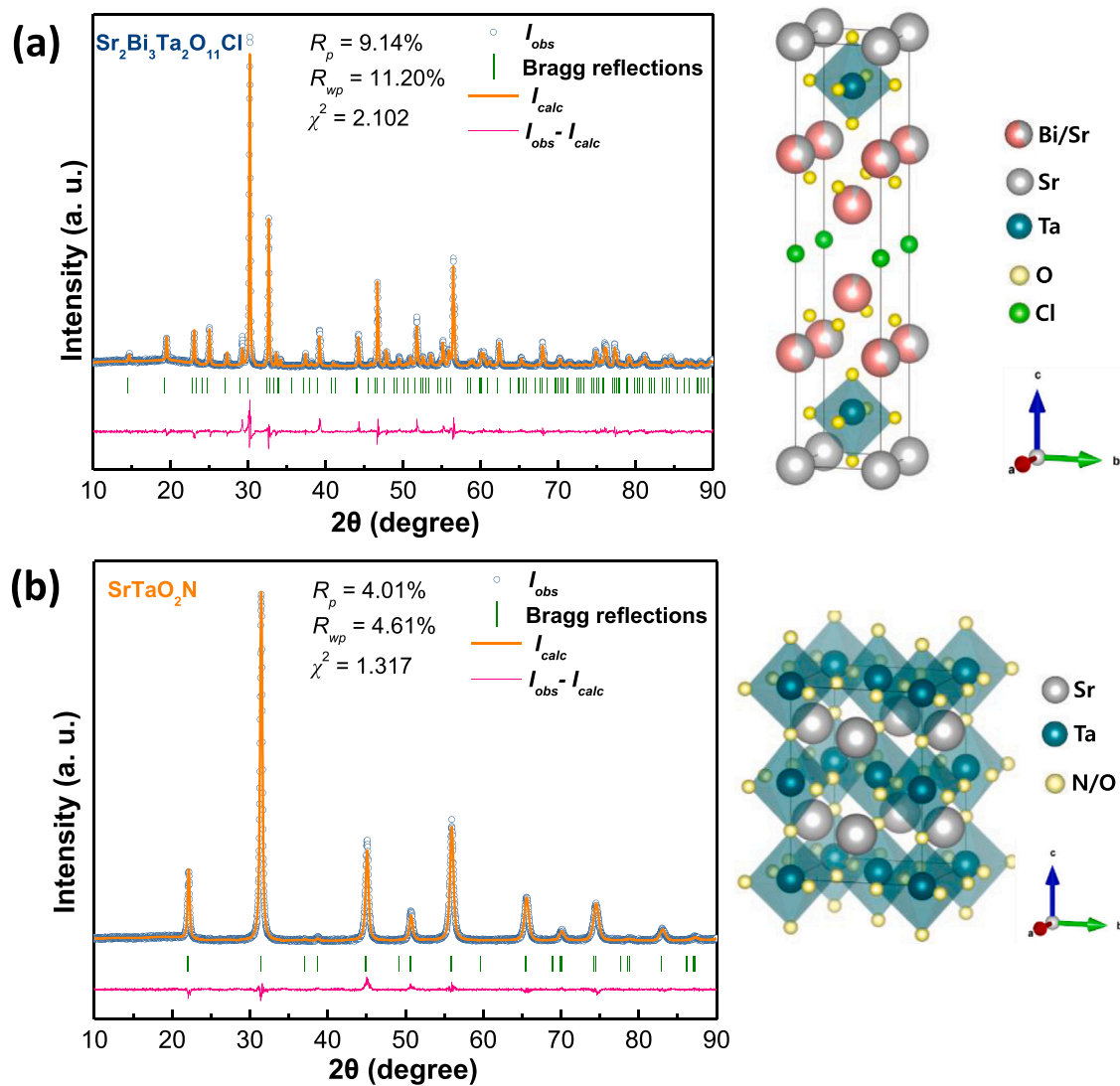


**Fig. 1.** Observed and calculated X-ray powder diffraction patterns for (a)  $\text{Sr}_2\text{Bi}_3\text{Ta}_2\text{O}_{11}\text{Cl}$  and (b)  $\text{SrTaO}_2\text{N}$ . The refinements all converge with reasonable  $R$  factors and  $\chi^2$  factor as shown in the insets. The refined crystal structures are displayed on the right; unit cell is marked by black lines. Here,  $R_p = 100 \times \sum |Y_{obs} - Y_{calc}| / \sum Y_{obs}$ ,  $R_{wp} = 100 \times \sum w |Y_{obs} - Y_{calc}|^2 / \sum w |Y_{obs}|^2$ ,  $\chi^2 = 100 \times \sum w |Y_{obs} - Y_{calc}|^2 / (N_{obs} - N_{var})$  and  $Y_{obs}$  = observed intensity,  $Y_{calc}$  = calculated intensity,  $N_{obs}$  = number of observations,  $N_{var}$  = number of variables.

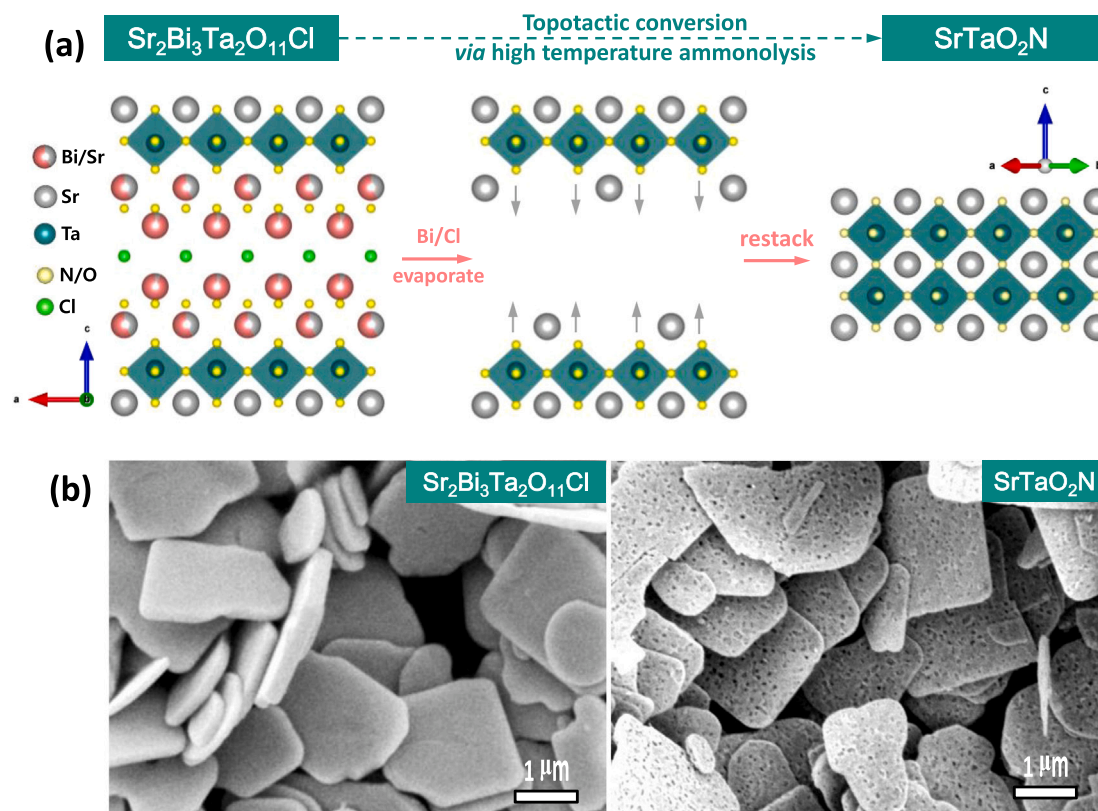


**Fig. 2.** (a) Schematic illustration of transform mechanism from  $\text{Sr}_2\text{Bi}_3\text{Ta}_2\text{O}_{11}\text{Cl}$  to  $\text{SrTaO}_2\text{N}$  via high-temperature ammonolysis. Crystal structures are oriented to clarify their relations:  $\text{Sr}_2\text{Bi}_3\text{Ta}_2\text{O}_{11}\text{Cl}$  along [010] direction;  $\text{SrTaO}_2\text{N}$  along [110] direction. (b) FE-SEM images of  $\text{Sr}_2\text{Bi}_3\text{Ta}_2\text{O}_{11}\text{Cl}$  (left) and  $\text{SrTaO}_2\text{N}$  (right).

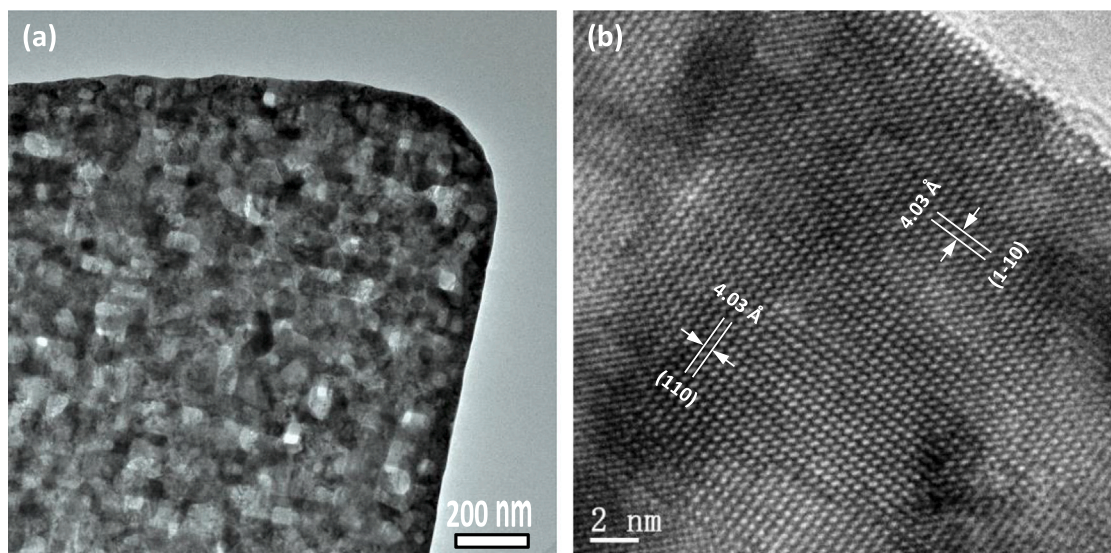


**Fig. 3.** (a) Transmission electron microscopy (TEM) image of SrTaO<sub>2</sub>N-P and (b) high-resolution TEM (HRTEM) image of SrTaO<sub>2</sub>N-P, the lattice fringes marked corresponds to (110) and (1–10) planes; thereby the top of SrTaO<sub>2</sub>N-P particle is oriented along [001] direction.

rationalized by the large structural differences between precursor and product that incurs substantial atom migrations/rearrangements during phase formation [43]. Uncontrolled grain growth prevails during phase formation, which in turn brings abundant grain boundaries in the polycrystalline product. For instance, SrTaO<sub>2</sub>N powders are rich in grain boundaries using traditional precursors for synthesis (e.g. Sr<sub>2</sub>Ta<sub>2</sub>O<sub>7</sub> or amorphous metal oxides, etc.) [44–46]. Nevertheless, previous studies have shown that perovskite oxynitride PSCs can be prepared if peculiar precursors are used for high-temperature ammonolysis [47].

In this work, SrTaO<sub>2</sub>N PSCs have been facilely prepared from a topotactic conversion route using Sr<sub>2</sub>Bi<sub>3</sub>Ta<sub>2</sub>O<sub>11</sub>Cl as the precursor. The as-prepared SrTaO<sub>2</sub>N PSCs deliver exceptional photocatalytic performance and robustness for O<sub>2</sub> production from water that clearly outperforms conventional SrTaO<sub>2</sub>N. When coupling SrTaO<sub>2</sub>N PSCs into a Z-scheme system, stable overall water splitting can be achieved that produces H<sub>2</sub> and O<sub>2</sub> in stoichiometry.

## 2. Experimental

### 2.1. Materials synthesis

#### 2.1.1. Preparation of SrTaO<sub>2</sub>N porous single crystals (PSCs)

SrTaO<sub>2</sub>N PSCs were synthesized by high-temperature ammonolysis of a double-layered Sillén–Aurivillius compound Sr<sub>2</sub>Bi<sub>3</sub>Ta<sub>2</sub>O<sub>11</sub>Cl as the precursor. Sr<sub>2</sub>Bi<sub>3</sub>Ta<sub>2</sub>O<sub>11</sub>Cl was prepared according to a previous report using SrBiO<sub>2</sub>Cl and SrBi<sub>2</sub>Ta<sub>2</sub>O<sub>9</sub> as the raw materials [48]. Briefly, BiOCl was firstly synthesized according to a previous procedure [49]. Subsequently, 0.5499 g freshly prepared BiOCl and 0.2982 g SrCO<sub>3</sub> (Aladdin, 99%) were thoroughly mixed and were calcined at 1073 K for 15 h to produce SrBiO<sub>2</sub>Cl. Furthermore, SrBi<sub>2</sub>Ta<sub>2</sub>O<sub>9</sub> was prepared by a polymerized-complex (PC) method. Specifically, 1.0000 g TaCl<sub>5</sub> (Aladdin, 99.95%), 1.3670 g Bi(NO<sub>3</sub>)<sub>3</sub>·5 H<sub>2</sub>O (Aladdin, 99%), 0.2952 g Sr(NO<sub>3</sub>)<sub>2</sub> (Aladdin, 99%) and 41.85 mmol of anhydrous citric acid (C<sub>6</sub>H<sub>8</sub>O<sub>7</sub>, Aladdin, 99.5%) were dissolved into 10 mL ethylene glycol (C<sub>2</sub>H<sub>6</sub>O<sub>2</sub>, Aladdin, 98%). A few drops of nitric acid were added to promote the dissolution of all chemicals. The so-formed solution was heated at 573 K on a hotplate under vigorous stirring until a brown resin was formed. The resin was calcined in air at 1073 K for 15 h in ambient air to produce SrBi<sub>2</sub>Ta<sub>2</sub>O<sub>9</sub>. For the preparation of Sr<sub>2</sub>Bi<sub>3</sub>Ta<sub>2</sub>O<sub>11</sub>Cl, 1.0418 g SrBi<sub>2</sub>Ta<sub>2</sub>O<sub>9</sub> and 0.3676 g SrBiO<sub>2</sub>Cl were mixed up with 0.5286 g NaCl (Aladdin, 99.5%) using an agate mortar and pestle. The admixtures were calcined at 1123 K for 15 h in ambient air and then cooled down to room

temperature at a rate of 7 K min<sup>−1</sup>. The resultant bright yellow mixture was washed thoroughly with water and absolute ethanol, centrifuged, and then dried at 353 K in an electric oven overnight.

The high-temperature ammonolysis of Sr<sub>2</sub>Bi<sub>3</sub>Ta<sub>2</sub>O<sub>11</sub>Cl was performed in a tube furnace under ultrapure NH<sub>3</sub> flow (300 mL min<sup>−1</sup>, Jiaya Chemicals, 99.999%) at 1273 K for 5 h. After cooling the furnace down to room temperature, the resultant powders were washed thoroughly with diluted hydrochloric acid and water, centrifuged, and dried at 353 K in an electric oven overnight. SrTaO<sub>2</sub>N synthesized by this route is denoted as SrTaO<sub>2</sub>N-P. For comparisons, SrTaO<sub>2</sub>N was also prepared using the conventional Sr<sub>2</sub>Ta<sub>2</sub>O<sub>7</sub> precursor. In brief, 1.4912 g SrCO<sub>3</sub> (Aladdin, 99.9%) and 2.2097 g Ta<sub>2</sub>O<sub>5</sub> (Aladdin, 99.9%) were mixed and calcined at 1273 K for 10 h in ambient air to produce Sr<sub>2</sub>Ta<sub>2</sub>O<sub>7</sub>. The freshly prepared Sr<sub>2</sub>Ta<sub>2</sub>O<sub>7</sub> was ammonolyzed under the same conditions with SrTaO<sub>2</sub>N-P except with a longer time of 20 h. The resultant SrTaO<sub>2</sub>N powders were denoted as SrTaO<sub>2</sub>N-S.

#### 2.1.2. Synthesis of Rh doped SrTiO<sub>3</sub> (SrTiO<sub>3</sub>:Rh)

Rh doped SrTiO<sub>3</sub>, i.e. SrTiO<sub>3</sub>:Rh, was prepared according to a previous report [50]. 0.5 wt% Ru was photo-deposited onto SrTiO<sub>3</sub>:Rh as a cocatalyst. In brief, 0.2 g SrTiO<sub>3</sub>:Rh powders (0.2 g) and RuCl<sub>3</sub> aqueous solution (1 mL, 1 mg·mL<sup>−1</sup>) were dispersed into methanol aqueous solution (20 mL, 50 vol%) with an aid of sonication. The so-formed suspensions were irradiated by a Xenon lamp (300 W, PLX-SXE300, Perfect Light) for a duration of 7 h.

### 2.2. Materials characterization

X-ray powder diffraction (XRD) experiment was conducted on a Bruker D8 Focus diffractometer (Bruker, Germany) to examine phase purity. Cu Kα<sub>1</sub> (λ = 1.5406 Å) and Cu Kα<sub>2</sub> (λ = 1.5444 Å) were used as the incident radiation. The general step size and duration time for data collection were set to be 0.01° and 0.1 s for each step, respectively. General Structure Analysis System (GSAS) software package was applied to perform Rietveld refinement on XRD data collected. The pseudo-Voigt function was used as the profile function and the first type Chebyshev polynomial was adopted for background fitting. An oxygen-nitrogen-hydrogen (ONH) analyzer (ONH836, LECO Co., USA) was used to determine the O and N content in the sample. Inductively coupled plasma optical emission spectrometry (ICP-OES, Agilent 720ES) was used to analyze the content of Sr and Ta in the sample. The optical absorbance of as-obtained samples was recorded on a UV-Vis



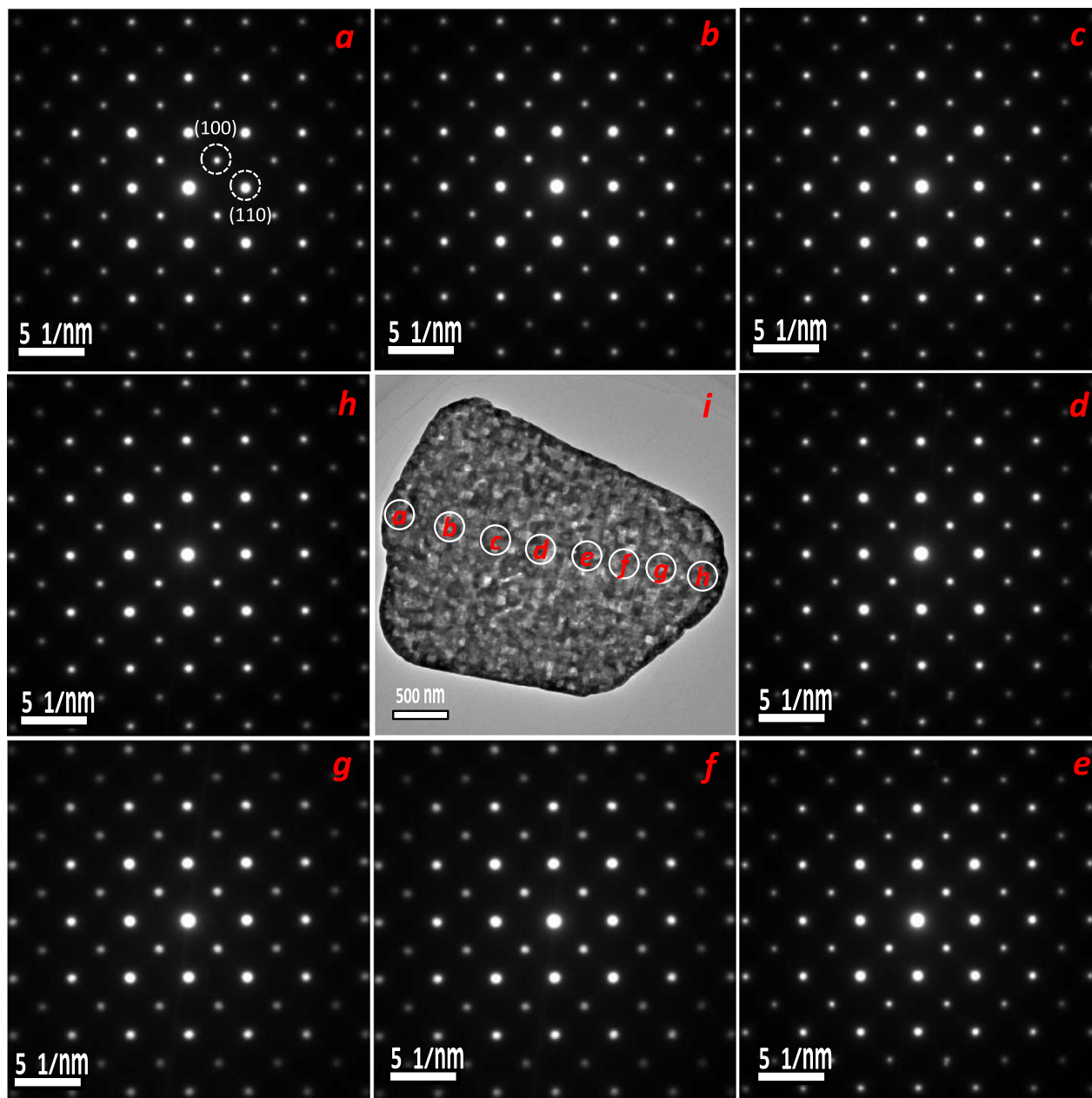


Fig. 4. Selected area electron diffraction patterns (a-h) for areas marked in a single SrTaO<sub>2</sub>N-P particle (i).

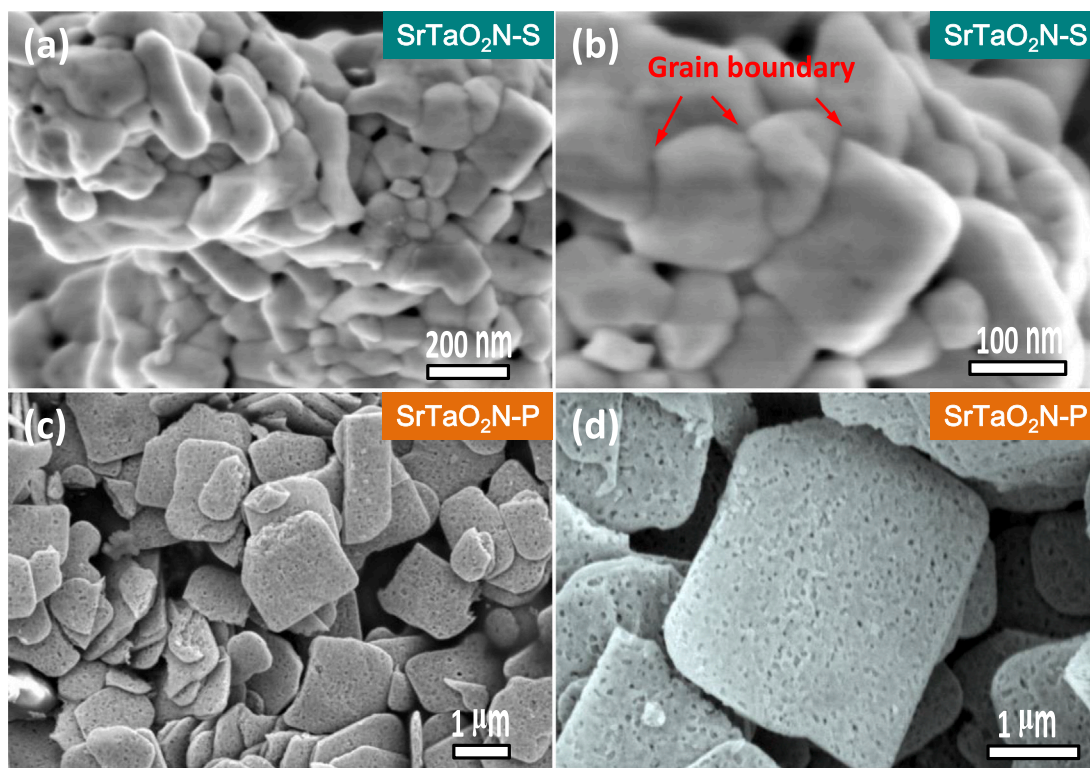


Fig. 5. Field-emission scanning electron microscopy (FE-SEM) images of SrTaO<sub>2</sub>N-S (a, b) and SrTaO<sub>2</sub>N-P (c, d).

spectrophotometer (JASCO-750, Japan) equipped with an integrating sphere in diffuse reflectance mode. BaSO<sub>4</sub> was used as the reference non-absorbing material, and the data collected were analyzed by the JASCO software suite. Microstructures of freshly prepared sample powders were inspected through a field emission scanning electron microscope (Hitachi S4800, Japan) equipped with a Mica energy-dispersive X-ray spectroscopy (EDS) analysis system, and a transmission electron microscope (TEM, JEOL JEM-2100, Japan). A NOVA 2200e adsorption instrument (Quantachrome, USA) was employed to analyze the specific surface areas of sample powders. The sample powders were pre-treated in vacuum at 473 K for 2 h and surface area was calculated based on the Brunauer–Emmett–Teller (BET) model. Surface conditions and valence band positions of sample powders were investigated by X-ray photoelectron spectroscopy (XPS, AXIS Ultra DLD, Japan) with a monochromatic Al K $\alpha$  X-ray source. All binding energy was referenced to adventitious carbon C 1 s peak at 284.7 eV and analyzed by XPS PEAKFIT software. The photoluminescence (PL) emission spectra were recorded on a FLUOROLOG-3-11 spectrophotometer in a liquid nitrogen bath ( $\sim 77$  K) with an excitation wavelength of 330 nm.

### 2.3. Photocatalytic experiment

Photocatalytic activity tests of all freshly prepared sample powders were conducted in a top-irradiation-type reactor connected to a gas-closed circulation and evacuation system (Labsolar-6A, Perfect Light). Typically, 100 mg sample powders loaded with proper amounts of CoO<sub>x</sub> were ultrasonically dispersed into 100 mL silver nitrate (0.05 M) aqueous solution. The so-formed suspension was transferred into the reactor and was evacuated for 45 min to remove air dissolved. 0.20 g La<sub>2</sub>O<sub>3</sub> (Aladdin, 99.9%) was also added into the reactor to control the pH value at ca. 8.5. A water jacket was used to stabilize reactor temperature at around 281 K. CoO<sub>x</sub> was deposited onto sample powders according to a previous report[47]: in brief, 100 mg sample powders were immersed into calculated amounts of cobalt nitrate aqueous

solution in an ultrasound bath. The resultant slurry was heated to 353 K in the air until dry, calcined under an NH<sub>3</sub> flow (flow rate  $\sim 300$  mL min<sup>-1</sup>) at 1023 K for 1 h, and re-calcined in the air at 473 K for another 1 h. A 300 W Xenon lamp (PLX-SXE300, Perfect Light) equipped with a UV cutoff filter ( $\lambda \geq 420$  nm) was used for generating visible light illumination. Bandpass filters at 420, 450, 500, 550, and 600 nm (Perfect Light) were applied to produce monochromatic light. The photon flux for each monochromatic light illumination is gauged using a quantum meter (Apogee MP-300, USA) and the gas component within the reactor was analyzed consecutively via an on-line gas chromatograph (GC2014C, SHIMADZU, Japan) with a TCD detector (5Å molecular sieve columns and Ar carrier). The apparent quantum efficiency was then calculated using the following equation:

$$AQE = \frac{4 \times \text{mol of oxygen production per hour}}{\text{mol of photon flux per hour}} \times 100\% \quad (1)$$

### 2.4. Photoelectrochemical experiments

Photoelectrodes of different samples were fabricated by electrochemically deposition method according to a previous report:<sup>6</sup> two pieces of fluorine-doped tin oxide (FTO) glass (30 × 10 mm) with the conductive sides facing inward were immersed into 50 mL anhydrous acetone solution containing 50 mg freshly prepared sample powders and 10 mg iodine (Sigma-Aldrich,  $\geq 99.8\%$ ). The two pieces of FTO glass were kept in parallel with a separation of 10 mm. A constant bias (10 V) was applied for 3 min under potentiostatic control (Keithley 2450 Source Meter, USA). The deposition area was around 1 cm<sup>2</sup>. The deposited FTO glass was then calcined at 673 K for 1 h under N<sub>2</sub> atmosphere (300 mL·min<sup>-1</sup>) to remove adsorbed iodine. A few drops of diluted TiCl<sub>4</sub> (Alfa-Aesar, 99.9%) methanol solution (10 mM) were dipped onto the glass which was then calcined at 623 K for 15 min in air. This procedure was repeated six times to minimize the exposure of naked FTO and to strengthen intergranular connections.

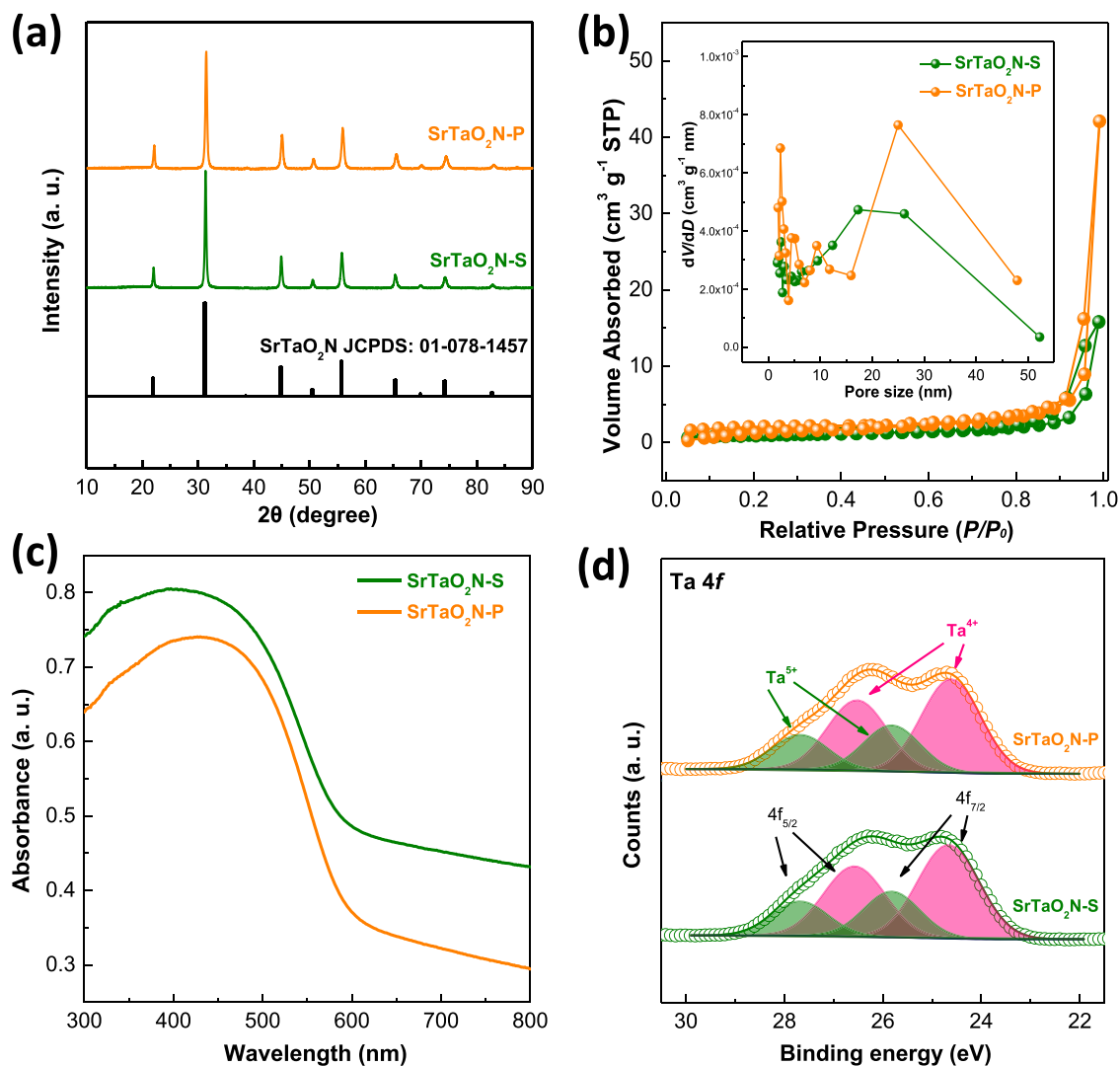


**Fig. 6.** (a) XRD patterns of SrTaO<sub>2</sub>N-S and SrTaO<sub>2</sub>N-P, SrTaO<sub>2</sub>N standard patterns (JCPDS: 01-078-1457) are also included; (b) BET surface area analysis of SrTaO<sub>2</sub>N-S and SrTaO<sub>2</sub>N-P, pore size distributions are included as inset; (c) UV-Vis DRS of SrTaO<sub>2</sub>N-S and SrTaO<sub>2</sub>N-P; (d) XPS Ta 4f spectra for SrTaO<sub>2</sub>N-S and SrTaO<sub>2</sub>N-P.

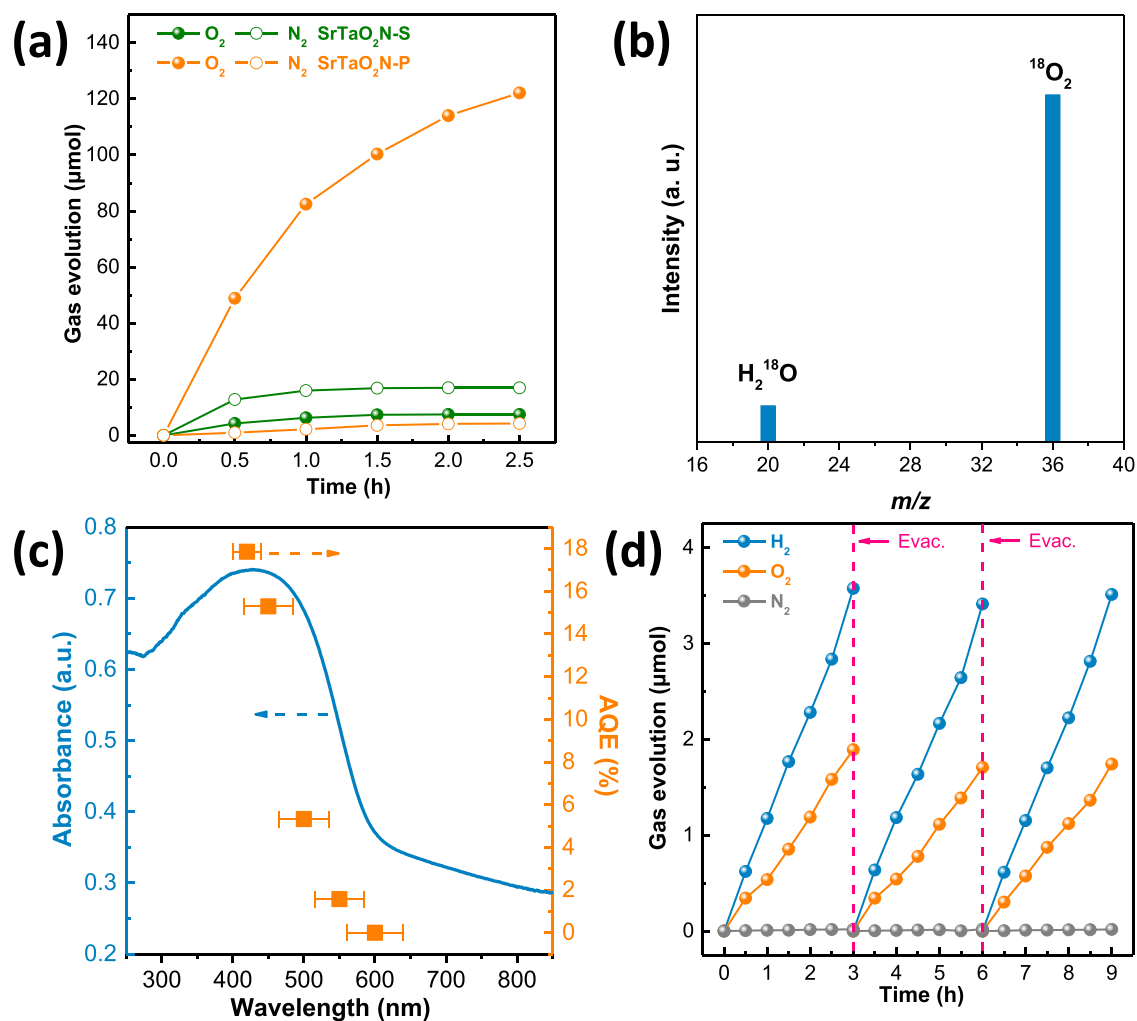


**Fig. 7.** (a) Temporal photocatalytic O<sub>2</sub> evolution over SrTaO<sub>2</sub>N-S and SrTaO<sub>2</sub>N-P under visible light illumination ( $\lambda \geq 420$  nm), 2 wt% CoO<sub>x</sub> was used as a cocatalyst and silver nitrate aqueous solution (0.05 M) was applied as an electron scavenger; (b) mass spectrum of gas evolved over SrTaO<sub>2</sub>N-P using H<sub>2</sub><sup>18</sup>O as the water resource under visible light illumination ( $\lambda \geq 420$  nm); (c) action spectra of SrTaO<sub>2</sub>N-P for photocatalytic O<sub>2</sub> production; (d) photocatalytic overall water splitting under visible light illumination ( $\lambda \geq 420$  nm) over a Z-scheme system containing SrTaO<sub>2</sub>N-P (loaded with 2 wt% CoO<sub>x</sub>) as the O<sub>2</sub>-evolution moiety and SrTiO<sub>3</sub>:Rh (loaded with 0.5 wt% Ru) as the H<sub>2</sub>-evolution moiety, Fe<sup>2+</sup>/Fe<sup>3+</sup> redox couple (0.02 M) was used as redox shuttle and evacuation was performed every 3 h.



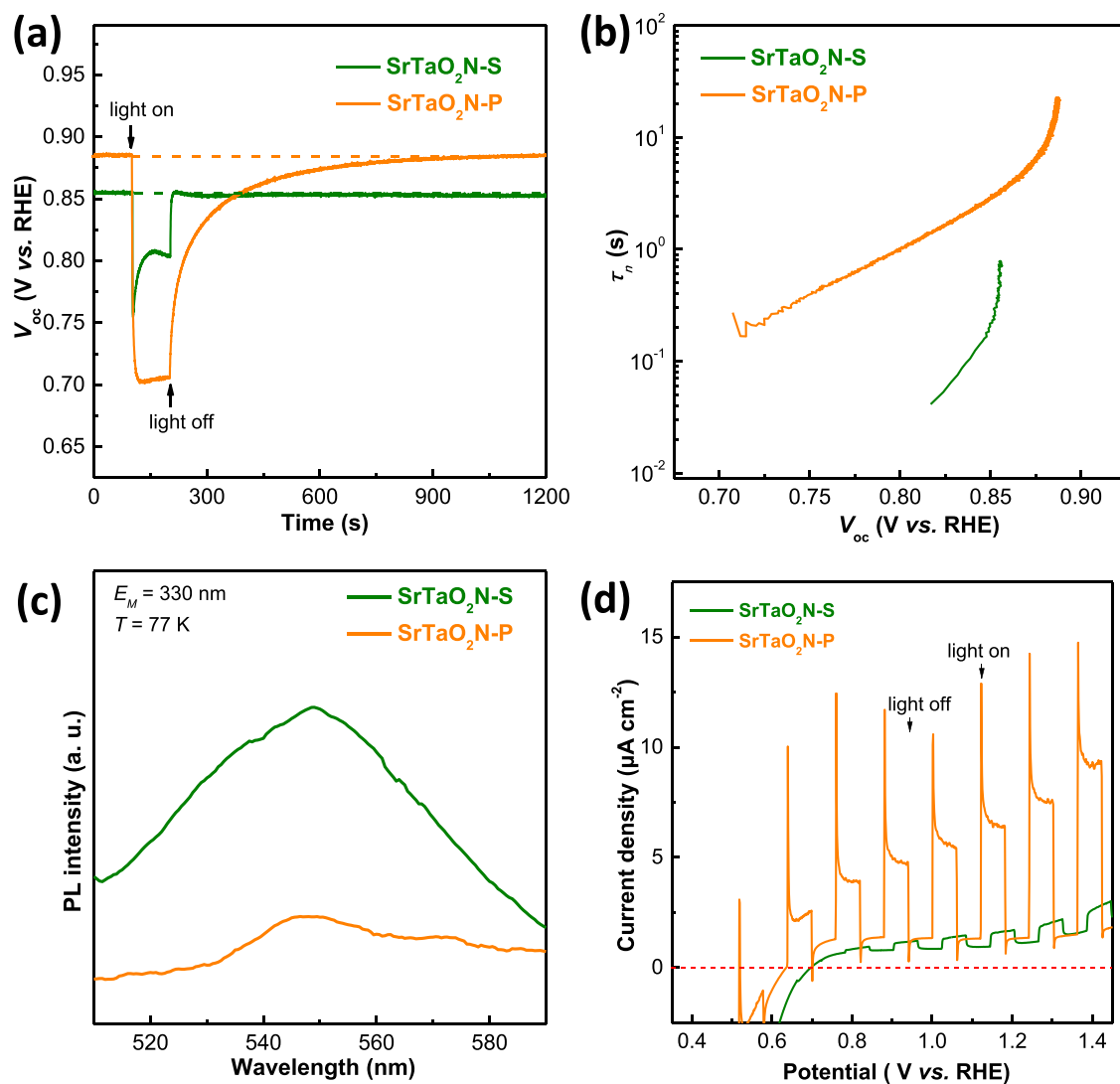


**Fig. 8.** (a) Open-circuit voltage decay profile in Ar for  $\text{SrTaO}_2\text{N-S}$  and  $\text{SrTaO}_2\text{N-P}$ , light illumination started once open-circuit voltage ( $V_{oc}$ ) was stabilized in the dark and was terminated after 100 s; (b) the electron lifetime derived from Eq. (1) as a function of  $V_{oc}$ ; (c) photoluminescence spectra of  $\text{SrTaO}_2\text{N-S}$  and  $\text{SrTaO}_2\text{N-P}$ , samples were excited by photons with a wavelength of 330 nm, and spectra were collected at 77 K; (d) linear sweep voltammetry of  $\text{SrTaO}_2\text{N-S}$  and  $\text{SrTaO}_2\text{N-P}$  under chopped visible light illumination ( $\lambda \geq 420$  nm).

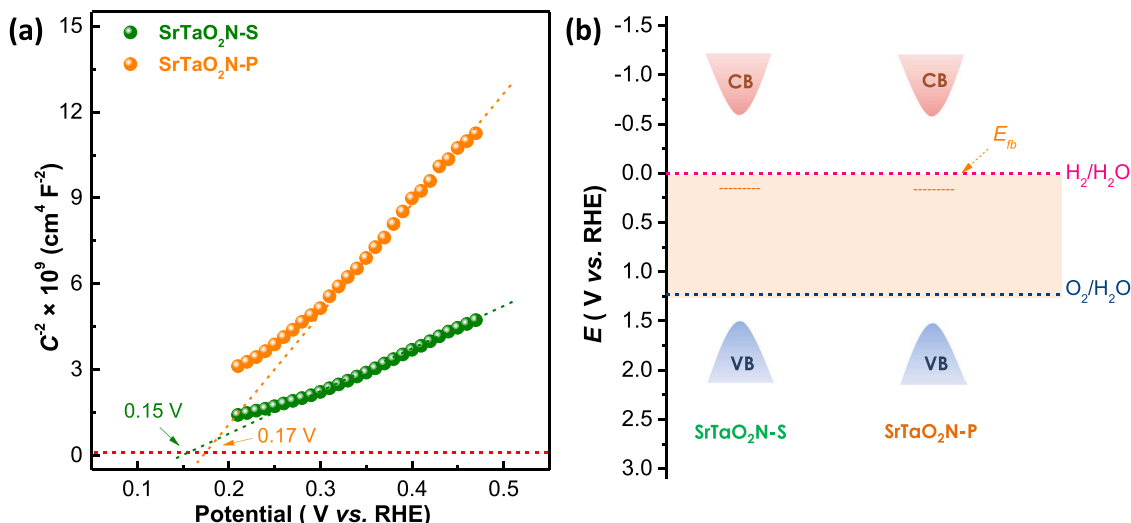


**Fig. 9.** (a) Mott-Schottky (MS) analysis of SrTaO<sub>2</sub>N-S and SrTaO<sub>2</sub>N-P, capacitance was extracted from impedance spectra at frequency of 1000 Hz. Flat band potential is determined by extrapolating the linear part of MS curves down to potential axis; (b) schematic illustration of band edge positions for SrTaO<sub>2</sub>N-S and SrTaO<sub>2</sub>N-P.

Photoelectrochemical measurements were carried out based on a three-electrode configuration setup connected to a Zahner electrochemical workstation. The photoelectrode, Pt foil (10 × 10 mm), and Ag/AgCl electrode were used as the working, counter, and reference electrodes, respectively. K<sub>3</sub>PO<sub>4</sub>/K<sub>2</sub>HPO<sub>4</sub> (25 mL, 0.1 M, pH = 12.66) was used as electrolyte and buffer. A 300 W Xenon lamp (PLX-SXE300, Perfect Light) coupled with a UV cutoff filter ( $\lambda \geq 420$  nm) was applied as the light source to produce visible light illumination. For Mott-Schottky (MS) analysis, impedance data at an AC signal of 1000 Hz with 10 mV amplitude was collected in the potential range of −0.2–0.5 V (vs. RHE). Capacitance values extracted from impedance data for MS analysis. Electrochemical impedance spectra were collected from 10<sup>5</sup> Hz to 0.1 Hz at open circuit voltage with amplitude of 10 mV. Open circuit voltage decay (OCVD) experiment was carried out in Ar using the same setup. The photoelectrode was stored in the dark first and illumination started once its open-circuit voltage ( $V_{oc}$ ) was stabilized. Light illumination was terminated after 100 s and decay of  $V_{oc}$  was recorded.

## 2.5. Theoretical calculation

Density functional theory (DFT) was introduced to calculate the electronic structures of SrTaO<sub>2</sub>N using a commercial Vienna ab initio simulation package. The calculation was performed using generalized gradient approximation (GGA) with Perdew, Burke, and Ernzerhof (PBE) exchange-correlation functional and projector augmented-wave pseudopotential. A tetragonal unit cell ( $a = b = 5.7$  Å,  $c = 8.1$  Å,  $\alpha = \gamma = \beta = 90^\circ$ ) was built for static electric potential calculations. Full relaxation of the structure was achieved until the force on each atom is less than 0.01 eV·Å<sup>−1</sup>. For static calculation, a 11 × 11 × 7 Monkhorst-Pack  $k$ -point grid was used with an energy cutoff of 500 eV. Geometry optimizations were performed with a 11 × 11 × 7 Monkhorst-Pack  $k$ -point grid until the total energies were converged to 10<sup>−5</sup> eV.

## 2.6. Simulation of photocarrier distribution in SrTaO<sub>2</sub>N under light illumination

COMSOL Multiphysics Semiconductor Module was introduced to simulate the photocarrier distribution in SrTaO<sub>2</sub>N particles under visible light illumination. The simulation was based on a two-dimensional (2D) brick model that considers the effect of grain boundaries and porosity. Particle transportation was numerically calculated using a finite volume method with Scharfetter-Gummel discretization[51]. For solid SrTaO<sub>2</sub>N

particles rich in grain boundaries, a model with compacted squares with a size of 100 nm was built. For porous SrTaO<sub>2</sub>N particles with grain boundaries, the model was modified by removing the square in the center to represent pores. For SrTaO<sub>2</sub>N porous single crystals, the model was further changed by deleting all internal interfaces among squares for the absence of grain boundaries. Semiconductor parameters used for calculation were tabulated in Table S1. Defect-assisted charge recombination, i.e. Shockley-Reed-Hall type was considered. The photocarrier generation within the model was set to be uniform since the random orientation of particles and multiple scattering/reflection homogenizes the light absorption and reduces the applicability of the Beer-Lambert law. The contact between neighboring squares was assumed to be a heterogeneous type to represent the situation of grain boundaries. The remaining interfaces were set to be pseudo Schottky type for the representation of semiconductor/electrolyte interfaces. Physics-controlled meshing was used to discretize the models which generate very fine mesh near the edges. The electrical simulation was performed by self-consistently solving the Poisson, drift-diffusion, and continuity equations for charge carriers at each discretized node.

## 3. Results and discussions

### 3.1. Structural evolution and microstructures

SrTaO<sub>2</sub>N PSCs are synthesized by high-temperature ammonolysis of Sr<sub>2</sub>Bi<sub>3</sub>TaO<sub>11</sub>Cl. Sr<sub>2</sub>Bi<sub>3</sub>TaO<sub>11</sub>Cl is a double-layer Sillén-Aurivillius type compound that contains intergrowth of regular Sillén- and Aurivillius-units along [001] direction [48]. The alignment of perovskite blocks in the Aurivillius-units is topotactically similar to those of SrTaO<sub>2</sub>N, as evidenced by Rietveld refinement (Fig. 1). The possible structural evolution mechanism from Sr<sub>2</sub>Bi<sub>3</sub>TaO<sub>11</sub>Cl to SrTaO<sub>2</sub>N is proposed in Fig. 2a. Since Bi/Cl evaporates from Sr<sub>2</sub>Bi<sub>3</sub>TaO<sub>11</sub>Cl during high-temperature ammonolysis, the residual perovskite blocks simply restack to form SrTaO<sub>2</sub>N without substantial atom migrations/rearrangements. This is clearly manifested by the topological relationship between Sr<sub>2</sub>Bi<sub>3</sub>TaO<sub>11</sub>Cl precursor and SrTaO<sub>2</sub>N product according to their field emission scanning electron microscopic (FE-SEM) images (Fig. 1b). The successful transformation from Sr<sub>2</sub>Bi<sub>3</sub>TaO<sub>11</sub>Cl to SrTaO<sub>2</sub>N (denoted as SrTaO<sub>2</sub>N-P) is also confirmed by UV-Vis diffuse reflectance spectra (UV-Vis DRS), and elemental mapping analysis (Figs. S1–S2). SrTaO<sub>2</sub>N prepared in this way not only maintains the plate-like particle morphologies but also contains a high porosity.

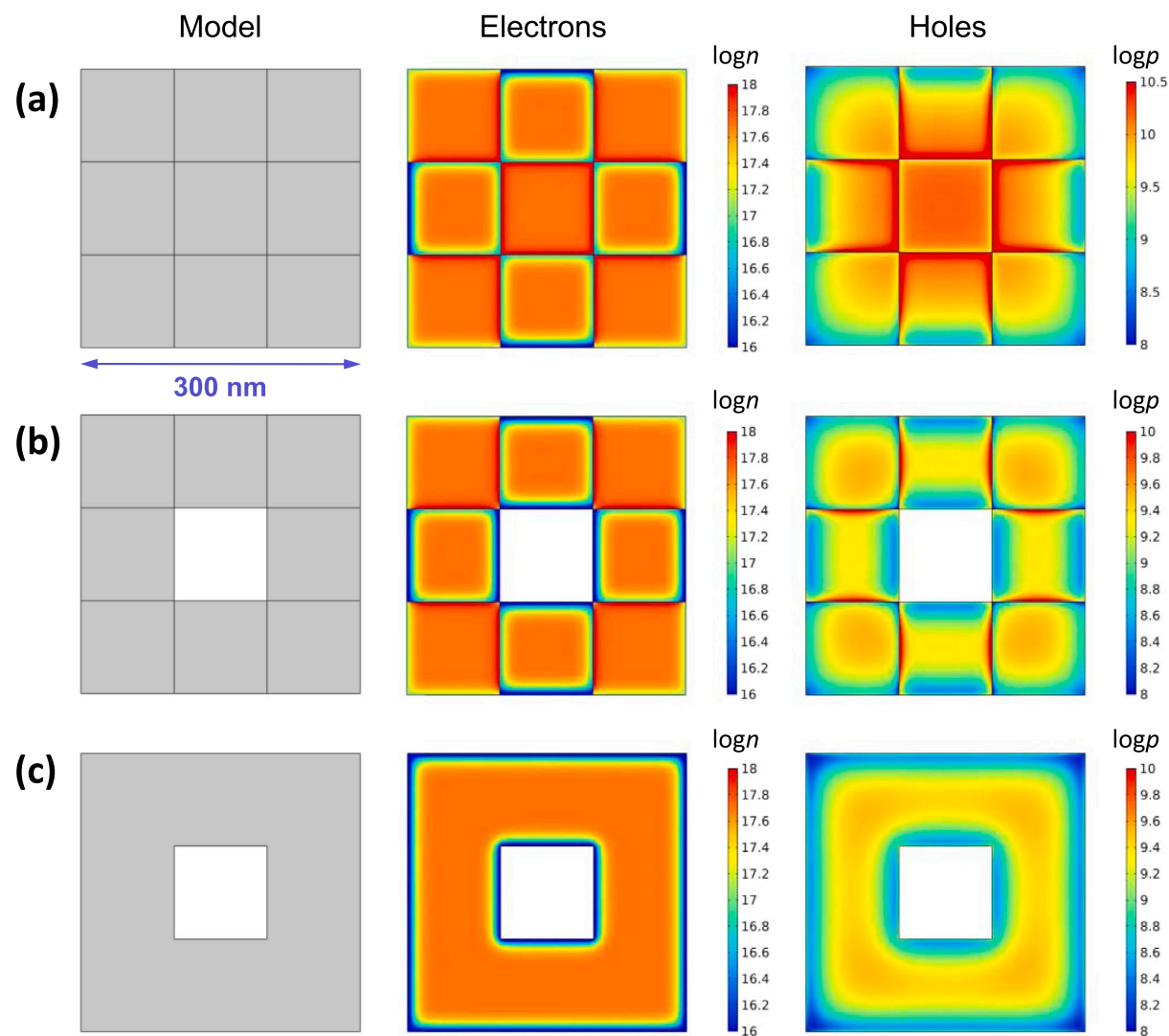


**Fig. 10.** Simulated photocarrier distribution in SrTaO<sub>2</sub>N particles with different microstructures by a two-dimensional brick model under light illumination: (a) solid particles with grain boundaries; (b) porous particles with grain boundaries; (c) porous single crystal without grain boundaries. Grain boundaries are represented by inner black lines in the brick models.

The particles of SrTaO<sub>2</sub>N-P are further investigated by transmission electron microscope (TEM). TEM study reveals that SrTaO<sub>2</sub>N-P owns peculiar microstructures that are free of grain boundaries and contain three-dimensionally inter-connected pores (Figs. 3, S3 and S4). The distribution of such porous architecture is quite uniform for the whole particle even though the particle size approaches several microns. More importantly, individual SrTaO<sub>2</sub>N-P particle preserves an identical crystal orientation at different areas of its porous skeleton, as evidenced by selected area electron diffraction (SAED) analysis (Fig. 4a-h). Thereby, SrTaO<sub>2</sub>N-P particles are indeed made up of PSCs rather than mesocrystals that are formed by piling up secondary particles. The top of these PSCs is all oriented along [001] direction, as revealed by SAED patterns (Fig. 4a) and high-resolution TEM image (Fig. 3b), being in good agreement with the proposed structural evolution mechanism. Such peculiar microstructures are completely different from SrTaO<sub>2</sub>N prepared by Sr<sub>2</sub>Ta<sub>2</sub>O<sub>7</sub> precursor (denoted as SrTaO<sub>2</sub>N-S) (Fig. 5). For instance, SrTaO<sub>2</sub>N-S comprises agglomerations of irregularly shaped particles that contain abundant grain boundaries (Fig. 5a and b).

### 3.2. Surface state and UV-Vis spectra

Although SrTaO<sub>2</sub>N-S and SrTaO<sub>2</sub>N-P have almost identical crystal structure and composition according to XRD and element analysis (Fig. 6a and Tables S1 and S2), they are different in surface areas. Thanks to the high porosity, SrTaO<sub>2</sub>N-P has a much higher surface area ( $\sim 6.5 \text{ m}^2/\text{g}$ ) than SrTaO<sub>2</sub>N-S ( $\sim 3.2 \text{ m}^2/\text{g}$ ) albeit the former owns a much larger particle size. The pore size for both samples is below 50 nm, suggesting that they are mesoporous materials. Nevertheless, SrTaO<sub>2</sub>N-P has a narrower pore size distribution than SrTaO<sub>2</sub>N-S, particularly in the range from 10 nm to 50 nm (Fig. 6b inset). UV-Vis diffuse reflectance spectra (UV-Vis DRS) suggest that both samples have strong absorption in the visible light region and have an absorption edge as far as 600 nm (Fig. 6c). Their bandgap values are similar ( $\sim 2.15 \text{ eV}$ ) according to Tauc plot analysis (Fig. S5) and are consistent with the value reported in the literatures [23,24,28,45]. The defective nature of the SrTaO<sub>2</sub>N surface is confirmed by X-ray photoelectron spectroscopy (XPS) analysis. The Ta 4f state of both samples reveals two distinct spin-orbit pairs corresponding to Ta<sup>5+</sup> and Ta<sup>4+</sup> species [32,52]. SrTaO<sub>2</sub>N-P and SrTaO<sub>2</sub>N-S are found to have similar Ta<sup>4+</sup> content at the surface according to XPS fitting data (Table S3). The XPS spectra for other elements are presented in Fig. S6 and are more or less the same for both samples. These results indicate that compared with conventional precursor Sr<sub>2</sub>Ta<sub>2</sub>O<sub>7</sub>, the new precursor Sr<sub>2</sub>Bi<sub>3</sub>TaO<sub>11</sub>Cl clearly modifies the microstructures of SrTaO<sub>2</sub>N but has little impact on the structure, composition, optical absorption, and surface state of the product SrTaO<sub>2</sub>N.

### 3.3. Photocatalytic performance and photocarrier separation

Given the peculiar microstructures of SrTaO<sub>2</sub>N-P, we continued to explore its photocatalytic properties. Control experiments that lack one of the following components, e.g. photocatalyst, water, and light illumination, did not produce any detectable O<sub>2</sub>, thereby precluding any spontaneous O<sub>2</sub>-evolution reactions. Upon visible light illumination ( $\lambda \geq 420 \text{ nm}$ ), only small amounts of O<sub>2</sub> were produced for SrTaO<sub>2</sub>N-S over 2.5 h (Fig. 7a). This result is in good accordance with previous reports that SrTaO<sub>2</sub>N generally exhibited a poor photocatalytic activity [28–30]. Moreover, significant amounts of N<sub>2</sub> (almost twice as those of O<sub>2</sub>) were produced along with O<sub>2</sub> evolution, indicating that SrTaO<sub>2</sub>N-S is indeed susceptible to photocatalytic self-decomposition. However, these situations were substantially changed for SrTaO<sub>2</sub>N PSCs. SrTaO<sub>2</sub>N-P produced up to 16 times more O<sub>2</sub> than SrTaO<sub>2</sub>N-S under identical conditions (Fig. 7a). The N<sub>2</sub> evolution, on the other hand, was also effectively inhibited. The good stability of SrTaO<sub>2</sub>N-P is supported by XPS analysis (Fig. S7) and a control experiment employing H<sub>2</sub><sup>18</sup>O as the water resource (Fig. 7b). Only <sup>18</sup>O<sub>2</sub> species were detected in this

case, indicating that the evolved O<sub>2</sub> stems exclusively from water-splitting reactions. These results highlight the importance of PSCs for the improvement of photocatalytic performance and stability under water oxidation conditions. The performance of SrTaO<sub>2</sub>N-P was further optimized by varying the amounts of CoO<sub>x</sub> cocatalyst loaded (Fig. S8). Under optimal conditions, SrTaO<sub>2</sub>N-P delivered apparent quantum efficiency (AQE) as high as 17.9% at  $420 \pm 20 \text{ nm}$ , being the highest one reported so far for SrTaO<sub>2</sub>N as an O<sub>2</sub>-evolution photocatalyst (Table S5). Meanwhile, action spectra reveal that AQE of SrTaO<sub>2</sub>N-P follows the trend of UV-Vis DRS spectra and has an onset around 600 nm (Fig. 7c), affirming that water oxidation over SrTaO<sub>2</sub>N-P is essentially photon-driven. On the other hand, the photocatalytic activity for H<sub>2</sub> production is still not satisfactory for both SrTaO<sub>2</sub>N-P and SrTaO<sub>2</sub>N-S (Fig. S9). Nevertheless, SrTaO<sub>2</sub>N-P shows a much better activity for H<sub>2</sub> production from water than SrTaO<sub>2</sub>N-S which is almost inert.

As water oxidation reactions are generally considered as the rate-limiting step for overall water splitting reactions, a high O<sub>2</sub>-evolution activity is very useful for the construction of a Z-scheme type photocatalytic system [53]. This is exemplified when coupling SrTaO<sub>2</sub>N-P with a H<sub>2</sub>-evolution photocatalyst, i.e. Rh doped SrTiO<sub>3</sub> (SrTiO<sub>3</sub>:Rh) [54]. The so-formed Z-scheme system is capable of stable overall water splitting with stoichiometric H<sub>2</sub> and O<sub>2</sub> production under visible light illumination ( $\lambda \geq 420 \text{ nm}$ ) (Fig. 7d).

Given the distinct photocatalytic behavior between SrTaO<sub>2</sub>N-S and SrTaO<sub>2</sub>N-P, we sought to investigate the separation conditions of photocarriers in these samples. First, we performed the open-circuit voltage decay (OCVD) experiments which offered a direct evaluation on the dissipation of photocarriers [55,56]. After terminating the light illumination, the open-circuit voltage ( $V_{oc}$ ) of SrTaO<sub>2</sub>N-S returned instantaneously to the value in the dark (Fig. 8a), indicating very fast photocarrier recombination in SrTaO<sub>2</sub>N-S. In contrast, a much longer time ( $> 600 \text{ s}$ ) was needed for a complete restoration of  $V_{oc}$  in the case of SrTaO<sub>2</sub>N-P, suggesting that the photocarriers were well-separated. The lifetime for the dissipation of photocarriers can be quantitatively accessed using the following equation [56]:

$$\tau_n = \frac{k_B T}{e} \left( \frac{dV_{oc}}{dt} \right)^{-1} \quad (1)$$

where  $\tau_n$  is the potential dependent lifetime,  $k_B$  is Boltzmann's constant,  $T$  is the temperature in K and  $e$  is the elementary charge. Apparently, SrTaO<sub>2</sub>N-P has a dissipation lifetime of nearly one order of magnitude longer than that of SrTaO<sub>2</sub>N-S (Fig. 8b), confirming that PSCs greatly improve separation conditions for photocarriers. This conclusion is also supported by photoluminescence (PL) spectra and photocurrent measurements (Fig. 8c and d). SrTaO<sub>2</sub>N-P has a much weaker PL signal and much higher photocurrent than SrTaO<sub>2</sub>N-S, indicative of a much easier dissociation of photocarriers. In addition, electrochemical impedance spectra suggest that SrTaO<sub>2</sub>N-P has a much smaller surface charge transfer resistance than SrTaO<sub>2</sub>N-S (Fig. S10), indicating facile photocarrier transfer at the surface of PSCs. It is noteworthy that SrTaO<sub>2</sub>N-S and SrTaO<sub>2</sub>N-P have similar band edge positions according to Mott-Schottky analysis (Fig. 9) and XPS valence band scan (Fig. S4e). Thereby, such a large difference in photocarrier separation arises most likely from the peculiar microstructures of PSCs.

### 3.4. Simulation of photocarrier distribution

For a better understanding of how PSCs promote photocarrier separation in SrTaO<sub>2</sub>N, we have simulated photocarrier distribution inside SrTaO<sub>2</sub>N particles using a two-dimensional (2D) brick model. These models are constructed by considering the contribution from grain boundaries and porosity. Information about these models and how simulation was performed can be found in the Supporting Information. Fig. 10 illustrates three representative models and their corresponding photocarriers distribution under visible light illumination. For solid



particles with grain boundaries, photocarriers tend to accumulate in the regions close to the grain boundaries (Fig. 10a), implying that grain boundaries are obstacles for photocarrier migration. In particular, buried particles are unlikely to participate in photocatalytic reactions as their photocarriers are mostly confined inside by surrounding grain boundaries. Introducing porosity into SrTaO<sub>2</sub>N particles, however, only partially mitigates the problem. The migration of photocarriers is still disrupted among neighboring particles and grain boundaries tend to store photocarriers (Fig. 10b). These results agree well with the poor photocatalytic activity of SrTaO<sub>2</sub>N-S and are helpful to explain the photocatalytic instability as holes accumulated at grain boundaries may trigger self-decomposition due to the presence of dangling bonds and/or nonstoichiometry at grain boundaries that favor side reactions. On the contrary, this situation can be fully resolved when all grain boundaries are removed as in the case of PSCs (Fig. 10c). All photocarriers are now liberated to migrate within the whole particle thereby resulting in the much-improved photocarrier separation conditions. These simulations explicitly elucidate how PSCs contribute to the separation of photocarriers and help to explain the high photocatalytic activity and good stability of SrTaO<sub>2</sub>N-P.

To further verify the critical role of grain boundaries, SrTaO<sub>2</sub>N-P powders were diced and sintered at high temperature to break up the PSCs architectures and create grain boundaries. The so-formed powders exhibit very poor photocatalytic activity for O<sub>2</sub>-evolution and continuously release N<sub>2</sub> under visible light illumination (Fig. S13). These results unambiguously indicate that grain boundaries are the key factor for the distinct activity and stability differences between SrTaO<sub>2</sub>N-P and SrTaO<sub>2</sub>N-S. The strategy to synthesize PSCs using Sillén–Aurivillius compound as a precursor can be well-extended to other perovskite oxynitrides. Take BaTaO<sub>2</sub>N for example, BaTaO<sub>2</sub>N PSCs can be facilely prepared using Ba<sub>2</sub>Bi<sub>3</sub>Ta<sub>2</sub>O<sub>11</sub>Cl as the precursor (Fig. S14), confirming the good applicability of the synthetic strategy.

#### 4. Conclusions

Porous single-crystalline SrTaO<sub>2</sub>N has been successfully synthesized by topotactically converting Sr<sub>2</sub>Bi<sub>3</sub>Ta<sub>2</sub>O<sub>11</sub>Cl via high-temperature ammonolysis. The SrTaO<sub>2</sub>N PSCs demonstrate superior activity and stability for photocatalytic O<sub>2</sub> production from water that clearly surpasses conventional SrTaO<sub>2</sub>N. Under optical conditions, the SrTaO<sub>2</sub>N PSCs deliver an AQE as high as 17.9% at 420 ± 20 nm, a record-breaking result for SrTaO<sub>2</sub>N-based O<sub>2</sub>-evolution photocatalyst. Overall water splitting with H<sub>2</sub>/O<sub>2</sub> equals 2 has also been attained in a Z-scheme system employing SrTaO<sub>2</sub>N PSCs as the O<sub>2</sub>-evolution moiety. Thanks to their peculiar microstructures, SrTaO<sub>2</sub>N PSCs own much-improved photocarrier separation conditions due to high porosity and absence of grain boundaries. These results not only justify the importance of PSCs for high photocatalytic activity but also extend the toolbox to improve conventional photocatalysts for efficient solar power utilizations.

#### CRediT authorship contribution statement

**Lin Yang:** Investigation, Formal analysis, Data curation. **Qingyang Fu:** Investigation, Methodology, Data curation. **Lina Wang:** Data curation, Software. **Jinxing Yu:** Data curation, Formal analysis. **Xiaoxiang Xu:** Conceptualization, Verification, Supervision, Funding acquisition, Writing – original draft.

#### Declaration of Competing Interest

The authors declare that they have no known competing financial interests or personal relationships that could have appeared to influence the work reported in this paper.

#### Acknowledgments

We thank the National Natural Science Foundation of China (Grant No. 51972233, 52172225), Natural Science Foundation of Shanghai (Grant No. 19ZR1459200), Shanghai Science and Technology Commission (14DZ2261100), the Fundamental Research Funds for the Central Universities for funding.

#### Appendix A. Supporting information

Supplementary data associated with this article can be found in the online version at doi:10.1016/j.apcatb.2021.120934.

#### References

- [1] S.S. Chen, T. Takata, K. Domen, *Nat. Rev. Mater.* 2 (2017) 17050.
- [2] Y.J. Dong, Q. Han, Q.Y. Hu, C.J. Xu, C.Z. Dong, Y. Peng, Y. Ding, Y.Q. Lan, *Appl. Catal. B-Environ.* 293 (2021), 120214.
- [3] F. Gao, R. Lei, X.Y. Huang, J. Yuan, C.K. Jiang, W.H. Feng, L.L. Zhang, P. Liu, *Appl. Catal. B-Environ.* 292 (2021), 120187.
- [4] X. Ma, G.W. Wang, L.F. Qin, J. Liu, B. Li, Y.A. Hu, H.F. Cheng, *Appl. Catal. B-Environ.* 288 (2021), 120025.
- [5] G.J. Yao, S. Yang, J.R. He, S.J. Jiang, C.Z. Sun, S.Q. Song, *Appl. Catal. B-Environ.* 287 (2021), 119986.
- [6] C.Q. Ji, W.J. Wang, E.M. El-Sayed, G.L. Liu, Y.N. Si, K.Z. Su, Z.F. Ju, F. Wu, D. Q. Yuan, *Appl. Catal. B-Environ.* 285 (2021), 119782.
- [7] W.C. Wang, Y. Tao, L.L. Du, Z. Wei, Z.P. Yan, W.K. Chan, Z.C. Lian, R.X. Zhu, D. L. Phillips, G.S. Li, *Appl. Catal. B-Environ.* 282 (2021), 119568.
- [8] X.X. Xu, C. Randorn, P. Efstathiou, J.T.S. Irvine, *Nat. Mater.* 11 (2012) 595–598.
- [9] X.X. Xu, G. Liu, C. Randorn, J.T.S. Irvine, *Int. J. Hydrog. Energ.* 36 (2011) 13501–13507.
- [10] Y. Tachibana, L. Vayssieres, J.R. Durrant, *Nat. Photonics* 6 (2012) 511–518.
- [11] J.A. Turner, *Science* 285 (1999) 687–689.
- [12] S. Zhu, X.F. Chen, Z.C. Li, X.Y. Ye, Y. Liu, Y. Chen, L. Yang, M. Chen, D.Q. Zhang, G. S. Li, H.X. Li, *Appl. Catal. B-Environ.* 264 (2020), 118515.
- [13] X.Y. Chen, H.Z. Sun, D.H. Kuo, A.B. Abdeta, O.A. Zelekew, Y.B. Guo, J.B. Zhang, Z. H. Yuan, J.G. Lin, *Appl. Catal. B-Environ.* 287 (2021), 119992.
- [14] R. Tahawy, E. Doustkhah, E.S.A. Abdel-Aal, M. Esmat, F.E. Farghaly, H. El-Hosainy, N. Tsunaji, F.I. El-Hosiny, Y. Yamauchi, M.H.N. Assadi, Y. Ide, *Appl. Catal. B-Environ.* 286 (2021), 119854.
- [15] Y.L. Li, C.L. Gao, W.S. Jiang, C.Q. Zhuang, W.Y. Tan, W.M. Li, Y.L. Li, L.H. Wang, X. Z. Liao, Z.C. Sun, J. Zou, X.D. Han, *Appl. Catal. B-Environ.* 286 (2021), 119923.
- [16] C.X. Zhao, Z.P. Chen, J.S. Xu, Q.Q. Liu, H. Xu, H. Tang, G.S. Li, Y. Jiang, F.Q. Zu, X. Lin, X.F. Yang, *Appl. Catal. B-Environ.* 256 (2019), 117867.
- [17] X.L. Chen, S.N. Xiao, H. Wang, W.C. Wang, Y. Cai, G.S. Li, M.H. Qiao, J. Zhu, H. X. Li, D.Q. Zhang, Y.F. Lu, *Angew. Chem. Int. Ed.* 59 (2020) 17182–17186.
- [18] T. Takata, J.Z. Jiang, Y. Sakata, M. Nakabayashi, N. Shibata, V. Nandal, K. Seki, T. Hisatomi, K. Domen, *Nature* 581 (2020) 411–414.
- [19] H. Kato, K. Asakura, A. Kudo, *J. Am. Chem. Soc.* 125 (2003) 3082–3089.
- [20] T. Hisatomi, J. Kubota, K. Domen, *Chem. Soc. Rev.* 43 (2014) 7520–7535.
- [21] K. Takane, *ACS Catal.* 7 (2017) 8006–8022.
- [22] B.B. Dong, J.Y. Cui, Y. Qi, F.X. Zhang, *Adv. Mater.* 33 (2021).
- [23] Y.I. Kim, P.M. Woodward, K.Z. Baba-Kishi, C.W. Tai, *Chem. Mater.* 16 (2004) 1267–1276.
- [24] S. Balaz, S.H. Porter, P.M. Woodward, L.J. Brinson, *Chem. Mater.* 25 (2013) 3337–3343.
- [25] H.C. Wang, J. Schmidt, S. Botti, M.A.L. Marques, *J. Mater. Chem. A* 9 (2021) 8501–8513.
- [26] Z.B. Chen, T.F. Jaramillo, T.G. Deutsch, A. Kleiman-Shwarsstein, A.J. Forman, N. Gaillard, R. Garland, K. Takane, C. Heske, M. Sunkara, E.W. McFarland, K. Domen, E.L. Miller, J.A. Turner, H.N. Dinh, *J. Mater. Res.* 25 (2010) 3–16.
- [27] Y.J. Zhong, Z.S. Li, X. Zhao, T. Fang, H.T. Huang, Q.F. Qian, X.F. Chang, P. Wang, S.C. Yan, Z.T. Yu, Z.G. Zou, *Adv. Funct. Mater.* 26 (2016) 7156–7163.
- [28] F. Oehler, S.G. Ebbinghaus, *Solid State Sci.* 54 (2016) 43–48.
- [29] M. Higashi, R. Abe, T. Takata, K. Domen, *Chem. Mater.* 21 (2009) 1543–1549.
- [30] M. Higashi, R. Abe, K. Teramura, T. Takata, B. Ohtani, K. Domen, *Chem. Phys. Lett.* 452 (2008) 120–123.
- [31] J.K. Zhou, C.G. Zhou, Z. Shi, Z. Xu, S.C. Yan, Z.G. Zou, *J. Mater. Chem. A* 6 (2018) 7706–7713.
- [32] H. Yu, J. Liu, W.J. Lan, S.C. Yan, P. Zhou, Y. Yang, H. Yu, *Cryst. Growth Des.* 20 (2020) 4307–4312.
- [33] Y.H. Hou, T.Z. Li, S.C. Yan, Z.G. Zou, *Appl. Catal. B-Environ.* 269 (2020), 118777.
- [34] T. Sakata, R. Yoshiyuki, R. Okada, S. Urushidani, N. Tarutani, K. Katagiri, K. Inumaru, K. Koyama, Y. Masubuchi, *Inorg. Chem.* 60 (2021) 4852–4859.
- [35] H.T. Huang, J.Y. Feng, H.W. Fu, B.W. Zhang, T. Fang, Q.F. Qian, Y.Z. Huang, S. C. Yan, J.W. Tang, Z.S. Li, Z.G. Zou, *Appl. Catal. B-Environ.* 226 (2018) 111–116.
- [36] J.D. Xiao, J.J.M. Vequizo, T. Hisatomi, J. Rabeah, M. Nakabayashi, Z. Wang, Q. Xiao, H.H. Li, Z.H. Pan, M. Krause, N. Yin, G. Smith, N. Shibata, A. Bruckner, A. Yamakata, T. Takata, K. Domen, *J. Am. Chem. Soc.* 143 (2021) 10059–10064.
- [37] J. Fu, F.Z. Wang, Y.Q. Xiao, Y.S. Yao, C. Feng, L. Chang, C.M. Jiang, V. F. Kunzelmann, Z.M. Wang, A.O. Govorov, I.D. Sharp, Y.B. Li, *ACS Catal.* 10 (2020) 10316–10324.

- [38] Y.Q. Xiao, C. Feng, J. Fu, F.Z. Wang, C.L. Li, V.F. Kunzelmann, C.M. Jiang, M. Nakabayashi, N. Shibata, I.D. Sharp, K. Domen, Y.B. Li, *Nat. Catal.* 3 (2020) 932–940.
- [39] P.A. Cox, *The Electronic Structure and Chemistry of Solids*, Oxford University Press, 1987.
- [40] C. Kittel, *Introduction to Solid State Physics*, 8th ed., Wiley, Hoboken, NJ, 2005.
- [41] J. Fu, S.E. Skrabalak, *Angew. Chem. Int. Ed.* 56 (2017) 14169–14173.
- [42] M. Hojamberdiev, H. Wagata, K. Yubuta, K. Kawashima, J.J.M. Vequizo, A. Yamakata, S. Oishi, K. Domen, K. Teshima, *Appl. Catal. B-Environ.* 182 (2016) 626–635.
- [43] W.D. Kingery, H.K. Bowen, D.R. Uhlmann, *Introduction to Ceramics*, John Wiley & Sons, Inc, New York, 1975.
- [44] A. Hosono, Y. Masubuchi, S. Kikkawa, *Ceram. Int.* 43 (2017) 2737–2742.
- [45] Y.I. Kim, *Ceram. Int.* 40 (2014) 5275–5281.
- [46] D. Li, L. Zeng, B. Li, X.J. Yang, Q.P. Yu, Z.S. Wu, *Mater. Des.* 187 (2020), 108416.
- [47] F.X. Zhang, A. Yamakata, K. Maeda, Y. Moriya, T. Takata, J. Kubota, K. Teshima, S. Oishi, K. Domen, *J. Am. Chem. Soc.* 134 (2012) 8348–8351.
- [48] A. Nakada, M. Higashi, T. Kimura, H. Suzuki, D. Kato, H. Okajima, T. Yamamoto, A. Saeki, H. Kageyama, R. Abe, *Chem. Mater.* 31 (2019) 3419–3429.
- [49] X. Zhang, Z.H. Ai, F.L. Jia, L.Z. Zhang, *J. Phys. Chem. C* 112 (2008) 747–753.
- [50] C.W. Dong, S.Y. Lu, S.Y. Yao, R. Ge, Z.D. Wang, Z. Wang, P.F. An, Y. Liu, B. Yang, H. Zhang, *Acs Catal.* 8 (2018) 8649–8658.
- [51] A.T. Garcia-Esparza, K. Takanabe, *J. Mater. Chem. A* 4 (2016) 2894–2908.
- [52] X. Wang, T. Hisatomi, Z. Wang, J. Song, J.L. Qu, T. Takata, K. Domen, *Angew. Chem. Int. Ed.* 58 (2019) 10666–10670.
- [53] A. Kudo, *MRS Bull.* 36 (2011) 32–38.
- [54] B. Moss, Q. Wang, K.T. Butler, R. Grau-Crespo, S. Selim, A. Regoutz, T. Hisatomi, R. Godin, D.J. Payne, A. Kafizas, K. Domen, L. Steier, J.R. Durrant, *Nat. Mater.* 20 (2021) 511–517.
- [55] B.H. Meekins, P.V. Kamat, *ACS Nano* 3 (2009) 3437–3446.
- [56] A. Zaban, M. Greenshtein, J. Bisquert, *ChemPhysChem* 4 (2003) 859–864.